Numerical investigation of blast-induced fractures using smoothed particle hydrodynamics

***†Saba Gharehdash, Luming Shen, and Yixiang Gan**

School of Civil Engineering, The University of Sydney, NSW 2006, Australia.

*Presenting author: saba.gharehdash@sydney.edu.au
†Corresponding author: saba.gharehdash@sydney.edu.au

Abstract

In this study, smoothed particle hydrodynamics (SPH) is utilized to simulate the dynamic behavior of rock under blast. In the simulation, the Johnson-Holmquist (JH2) damage model is employed to model the rock damage and fracture under blasting loads. The effects of air and water as coupling material and copper inside of the borehole are considered. A penalty based node to node contact model is introduced on the interfaces of the different SPH parts to avoid interface effects. The simulated 3D blast-induced fractures are validated by comparing with available experiments. It is found that the crack propagation is asymmetrical around the borehole, despite the apparent isotropy and homogeneity of the simulated rock. The numerical results indicate that the SPH approach used in this work can be applied to effectively simulate densely cracked region, radial cracks and circumferential cracks of rock subjected to blast loading.

Keywords: smoothed particle hydrodynamics, blast loading, fracture, rock

Introduction

Blast-induced damage in rock is a significant yet poorly understood area in the hydrogeology [1], coal gasification [2], geothermal reservoirs [3], fracturing oil shale with explosives [4] and mining [5]. The prediction and control of blast damage has been traditionally done by approximate methods mostly based on experience rather than on understanding of the physical phenomenon. Perhaps the difficulties of experimentation and modeling in blasting added to the significant imperfections of natural rock masses at every scale, plus the limited knowledge on material behavior at very large stresses and loading rates, has significantly limited the research in this area and therefore its understanding. The study presented in this paper intends to contribute to this knowledge by providing a method to be applied to predict blast-induced damage in rock.

Among the different methods which are used for this complicated problem, computational methods are the most economical and efficient tool [6]. Zhu et al. [5] conducted a FEM method of blasting-induced damage in cylindrical rocks, Potyondy et al. [7] applied PFC3D, a 3-dimensional discrete-element program, to simulate rock fragmentation. Trivino and Mohanty [8] used a combined finite-discrete element method (FEM–DEM) to simulate blast-induced damage in a granitic outcrop. The numerical models presented in their works can be applied to treat the problem of blasting-induced crack initiation and propagation in rocks. Three basic fracture zones, i.e., crushed zone, severely fractured zone and spalling cracks have been successfully simulated. However, they could not extend their works to verify the predicted fracture dimension against controlled experiment. Their approach holds promise for this class of rock fracture problems. While the quantitative correlations of model predictions with experiment was not successful.

The mesh free methods such as smoothed particle hydrodynamics (SPH) [9], material point method [10] and discrete element method [11] have shown the potentials to simulate large deformation behaviour of rock medium by including elasto-plastic or damage models. In particular, SPH is widely applied to computational solid mechanics [9] due to its superiority in solving problems with large deformation. Recent developments in SPH make it promising for simulating rock fracture and fragmentation under blast load [12]. The numerical example presented in their work showed the potentiality to estimate blast-induced crack initiation and propagation. The failure process of the rock medium can be separated into three failure zone namely, crush zone, radial cracks zone and spalling cracks zone. In many applications, it is convenient to combine SPH with another method, such as the finite element (FEM) or discrete element method (DEM) [13, 14]. Gharehdash et al. [13] used coupled SPH-FEM for investigating of rock fracturing. Presented SPH-FEM approach can be applied to treat the problem of blasting-induced crack propagation. It was found that the model is capable to capture some of the observed phenomena in rock blasting experiments. SPH-FEM approach may potentially lead to handling of large deformation problems with low computational cost, however, the interaction between SPH particles and FEM elements didn’t represent the real interface between SPH and FEM. SPH-DEM for first time was used by Fakhimi and Lanari [14]. It was shown that the proposed hybrid model is capable of simulating the crack propagation in the rock material and the crushed zone and radial cracks, and surface spalling were all captured successfully. The interaction between DEM and SPH followed a perfectly plastic collision that caused partial penetration of smoothed particles into discrete elements. The contact model in hybrid methods can be problematic and cause numerical instability.

Although some realistic features such as the incorporation of various free surfaces and displacement of fragments have been achieved in 3D simulations, most previous investigations considered only 2D simulations [5]. In the present work, a 3D numerical simulation using SPH has been performed to predict the fracture patterns in rock under different blast conditions. The numerical investigation in this paper considers both quantitative and qualitative aspects of rock blasting.

Methodology

Smoothed particle hydrodynamics method

Smoothed Particle Hydrodynamics (SPH) is a Lagrangian-based numerical method used for simulating problems in fluid and solid mechanics. SPH was first developed to simulate nonaxisymmetric phenomena in astrophysical dynamics [15]. Due to its flexibility of meshless Lagrangian nature, ease of implementation is well employed within numerous branches of computational physics [9].
The SPH method considered as an interpolation method using the sifting property of the Dirac-delta function. Figure. 1 shows a particle neighbourhood domain centred at a particle of interest, labelled *i*. The circle of radius *2h* indicates the immediate neighbours.

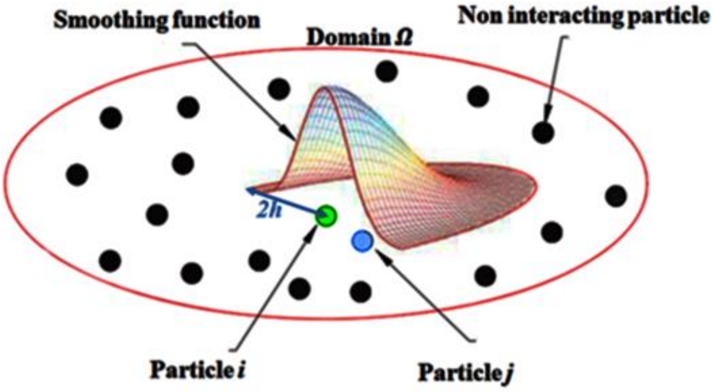

Figure 1. SPH particle neighborhood.

Consider a function *f*, a kernel *W* which has a width (support domain) determined by the parameter *h*, we define the kernel estimate as

$$f(x) = \int f(x_j) W(|x - x_j| / h) dx_j \tag{1}$$

where x_j is the value of the quantity *x* for particle *j*, *h* is smoothing length. If we go from an integral to a sum, then the discrete kernel estimate becomes the summation over neighbouring particles and the particle *i* itself as

$$f(x) \cong \sum_{j=1}^{N} m_j f(x_j) W(\left|x - x_j\right| / h) / \rho_j \tag{2}$$

where m_j is mass of particle *j*, ρ_j is density of particle *j* and *N* is the number of particles within support domain of kernel function. Particle equation for the gradient can be obtained as

$$\nabla f(x)_{x \approx x_j} \cong -\sum_{j=1}^{N} m_j f(x_j) \nabla W(\left|x - x_j\right| / h)_{|x \approx x_j} / \rho_j \tag{3}$$

Approximations (2) and (3) to functions and their derivatives allows estimates of accelerations, strain rates, etc., in the continuum equations and forms the basis of SPH. The transformation of conservation equations of continuum mechanics into SPH framework described as

$$\frac{d\rho_i}{dt} = \rho_i \sum_j \frac{m_j}{\rho_j} \left(U_j - U_i\right) \cdot \nabla W_{ij} \tag{4}$$

$$\frac{dU_i}{dt} = \sum_j m_j \left(\frac{\sigma_i}{\rho_i^2} + \frac{\sigma_j}{\rho_j^2} - \Pi_{ij} I + \left(R_{\varepsilon i} + R_{\varepsilon j}\right) f_{ij}^n \right) \cdot \nabla W_{ij} \tag{5}$$

$$\frac{d\rho_i}{dt} = \rho_i \sum_j \frac{m_j}{\rho_j} \left(U_j - U_i\right) \cdot \nabla W_{ij} \tag{6}$$

where *I* is unit matrix, *U* is the velocity vector, and σ is the stress tensor. A given particle *i* has a density change determined by (4), an acceleration obtained from (5), and an internal energy change given by (6). The Π_{ij} term represents the artificial viscous pressure. The summations are over neighbouring *j* particles. For more comprehensive details on SPH method one can refer to Gingold and Monaghan [15].

SPH simulations

In the present study, SPH algorithm was implemented into the explicit finite element code LS-DYNA [16] in order to model rocks failure under blast loading. Some modifications in the SPH suit the needs of simulations in removing the tensile instability, interaction between different SPH parts and artificial viscosity. The proposed SPH is then applied to the simulation of well documented laboratory experiments in granitic rocks. The different aspects of SPH are described as follows. In order to prevent the particle from clumping with neighbour particles we used the most effective and successful treatment which was introduced by Monaghan [17]. The main idea is to introduce an artificial repulsive force in the neighbourhood of a SPH particle that is in tension. The repulsive force is introduced in the momentum equation in the form of an artificial stress term (Eq. 5). In Equation 5 $R_{\varepsilon i}$ and $R_{\varepsilon j}$ are artificial stress terms of particles *i* and *j*, respectively, with correction parameter ε [17]; *n* is exponent dependent on the smoothing kernel; and f_{ij} is defined as

$$f_{ij} = \frac{W_{ij}}{W(\Delta d, h)} \tag{7}$$

Where Δd is initial particle spacing. In this study, h is assumed to be $1.2\,\Delta d$ for the cubic spline kernel. For the problem described herein, exponent n and correction parameter ε are chosen to be 4 and 0.5, respectively, to remove the tensile instability of the SPH particle of the rock material [17]. This is of the greatest importance for applications in solid mechanics, and especially for problems involving damage, fracture and fragmentation resulting from transient tensile stress fields. On the other hand, Smoothed quantities of a particle show falsified values when densities and masses of neighbouring particles vary largely within the smoothing length. So in our blast simulations, a penalty based node to node contact model is introduced on the interfaces of the different SPH parts to avoid interface effects. The standard SPH method is based on an updated Lagrangian formulation. Rabczuk et al. [18] has shown that this updating of the coordinates was the main source of instability in solid mechanics applications. He hence proposed to use a total Lagrangian formulation of the equilibrium equations [18]. This formulation was used for updating the equilibrium equations in this work.

Description of simulated problem

For blast simulation a cylindrical rock containing a single centrally located line source of explosive coupling with different medium is considered (see Figure 2). The cylindrical rock measures 144 mm in diameter and 150 mm in length. The line source of explosive is represented by a single strand of detonating cord containing a core load of PETN explosive (1.65 mm in diameter) surrounded by a thin sheath of polyethylene, with the total diameter of 4.5 mm. The borehole diameter is 6.45 mm. The coupling materials of water and air are used in this simulation. A copper tube with a 1.2 mm thick was tightly installed in the borehole of each specimen. Copper can be deformed easily under the applied shock/stress loads and expand with the borehole without tearing, and thereby preventing any gas penetration into the resulting cracks to prevent fragmentation of rock. Figure 2 shows three dimensional view of rock specimen with a scaled close-up of the borehole region for different simulations.

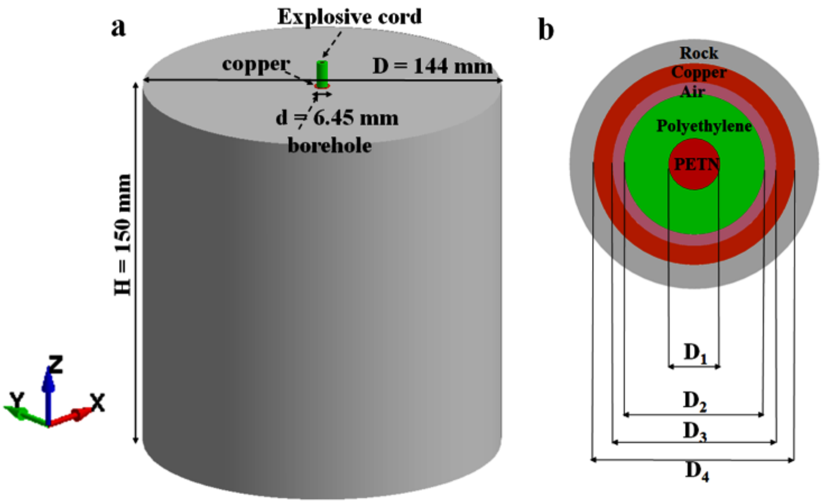

Figure 2. Rock cylinder under blast load a) 3D view, b) cross-section view of the borehole.

The p-wave velocity in the Barre granite is calculated with the following expression:

$$c_d = \sqrt{\frac{(\lambda + 2\gamma)}{\rho}} \tag{8}$$

where λ and γ are Lame constants and ρ is the material's mass density. This wave velocity is used for analysis of wave propagation in the numerical simulations. The transmitted pressure arrival from the top of the borehole is used to record arrival of the stress wave from blasting. The rock bottom and top surfaces are set as the fixed boundary in the Z direction, and its side surface is set as the free boundary. The location of the initiation points was set at the top of the blast hole. After mesh convergence study, particle distance of 0.15 mm was selected for dynamic simulation, giving a total 5457876 particles. Table 1 depicts all combinations of borehole diameters, detonating cords and coupling media used in the simulations.

Table 1. Different combinations of detonating cords, coupling media and borehole diameter (equal to outside diameter of copper tube)

Materials inside of borehole	Simulations		
	Air-coupled	Water-coupled	Without copper
	Outside diameter (mm)		
PETN (D_1)	1.65 mm	1.65 mm	1.65 mm
Polyethylene (D_2)	4.5 mm	4.5 mm	4.5 mm
Air (D_3)	5.25 mm	-	6.45 mm
Water (D_3)	-	5.25 mm	-
Copper (D_4)	6.45 mm	6.45 mm	-

Material model

In the SPH simulations, Johnson-Holmquist constitutive model [19] was used to model granitic rocks. This damage model is capable of considering pressure and strain rate dependencies, and allows softening of the material under investigation. A brief description of the model can be found in Johnson and Holmquist [19]. The material properties of the Barre granite rock for blast simulation is from Dehghan Banadaki and Mohanty [20]. Johnson and Cook model [21] was used to model the copper. This model requires an equation of state (EOS) to be incorporated to represent the behaviour of the copper under different phases, so Mie-Grunesien EOS was used for copper under shock load [21]. For air, water and polyethylene Material Type 9 of LS-DYNA (*MAT_NULL) [16] is used. As for the air, the polynomial EOS is usually employed, in which the pressure P is expressed as

$$p = C_0 + C_1\mu + C_2\mu^2 + C_3\mu^3 + \left(C_4 + C_5\mu + C_6\mu^2\right)e \tag{9}$$

where e is the internal energy per volume. The compression of the material is defined by the parameter $\mu = \frac{\rho}{\rho_0} - 1$, where ρ and ρ_0 are the current and initial density of the material, respectively. As a matter of fact, the air is often modelled as an ideal gas by setting $C_0 = C_1 = C_2 = C_3 = C_6 = 0$ and $C_4 = C_5 = 0.401$. Air mass density ρ_0 and initial internal energy e_0 are 1.255 kg/m^3 and 0.25 J/cm^3, respectively. For the water and polyethylene (sheath of the detonating cord) in the immediate vicinity of the explosive charge, shock EOS is used [20]

$$U_s = C_0 + su_p \tag{10}$$

where U_S is the shock wave velocity, C_0 is the bulk sound speed, u_p is the particle velocity and s is the material constant, listed in Table 2.

Table 2. Shock EOS parameters for the water and polyethylene used in the simulations [20].

Material	Bulk sound speed C_0 (m/s)	Material constant s
Polyethylene	2901	1.481
Water	1483	1.750

The explosive PETN was modelled using explosive burn constitutive model (*MAT_HIGH_EXPLOSIVE_BURN) [16]. For the detonation produced explosive gas, the standard Jones-Wilkins-Lee (JWL) equation of state is employed, which corresponds to a detonation velocity of 6690 m/s and a Chapman–Jouget (C-J) pressure of 16 GPa. The pressure of the explosive gas is

$$p = A\left(1 - \frac{\omega\eta}{R_1}\right)e^{-\frac{R_1}{\eta}} + B\left(1 - \frac{\omega\eta}{R_2}\right)e^{-\frac{R_2}{\eta}} + \omega\eta\rho_0 E \tag{11}$$

where η is the ratio of the density of detonation products to the initial density of the original explosive, E is the specific internal energy per unit mass, and A, B, R_1, R_2, ω are fitting coefficients. The values of the corresponding coefficients can be found in [20].

Simulations of blast testing

A mesh convergence study is conducted first. Comparisons of the fracture patterns for the different mesh sizes are presented in Figure 3. Six models, shown in Figure 3, with varying SPH mesh densities were created to compare the sensitivity of the predicted fracture pattern response to mesh size. Six meshes with particle sizes 0.6, 0.4, 0.25, 0.2, 0.15 and 0.1 mm for top cross section are modelled. It can be noticed that the crack patterns are very similar for particle sizes 0.25, 0.2, 0.15 and 0.1 mm although the crack paths are thinner for the finer meshes. The failure patterns for the four mesh densities are similar and there is failure pattern convergence as the mesh size decreases. Considering the balance between accuracy and efficiency, the mesh size 0.15 mm is used in all the simulations below. This mesh density study clearly illustrates the importance of performing a mesh study using the SPH method.

Four different simulations for rock under blast loading were performed as described in Table 1. In this section, we first show the pressure history results for air-coupled with copper simulation to validate the proposed SPH, and then analyse the crack patterns produced by the blast loading. Pressures at different distances from the borehole walls obtained from numerical simulations are shown in Figure 4. As seen, the simulated pressure distribution match the experimental data quite well.

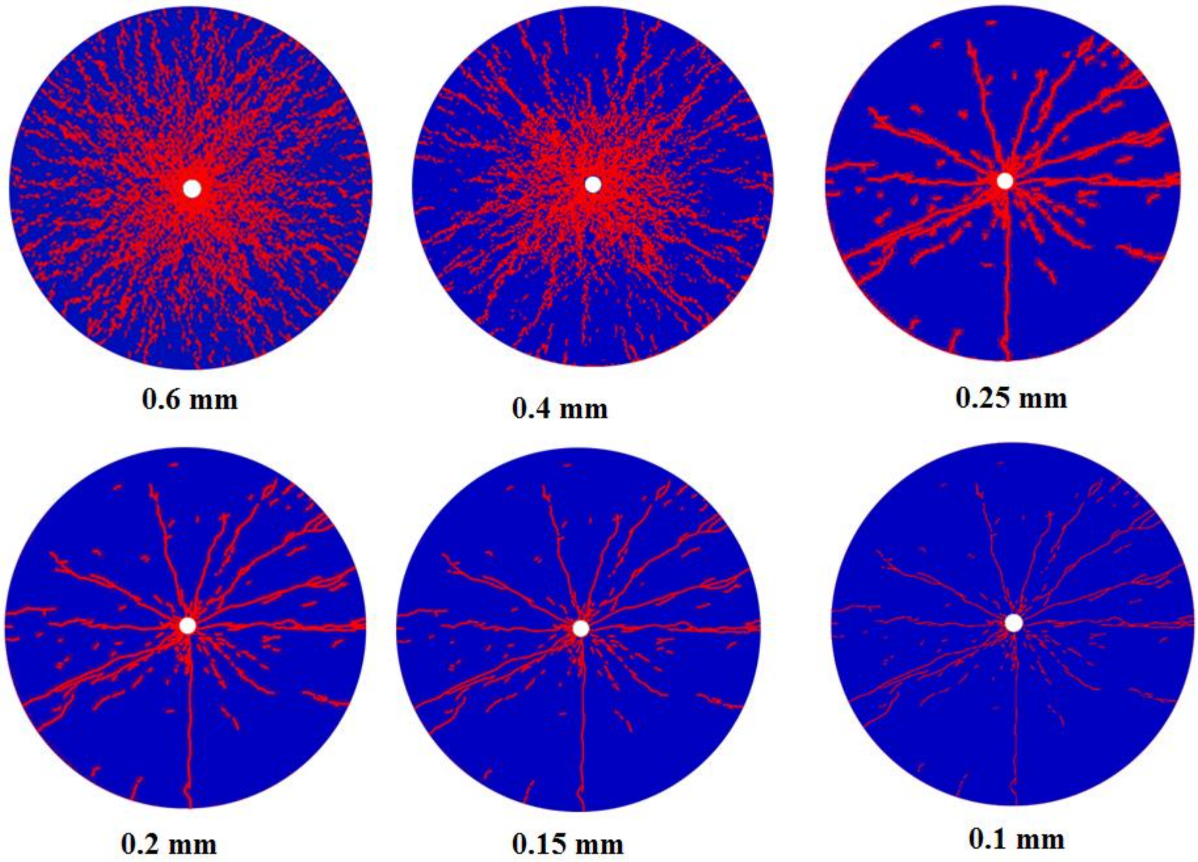

Figure 3. Failure patterns simulated using different mesh sizes.

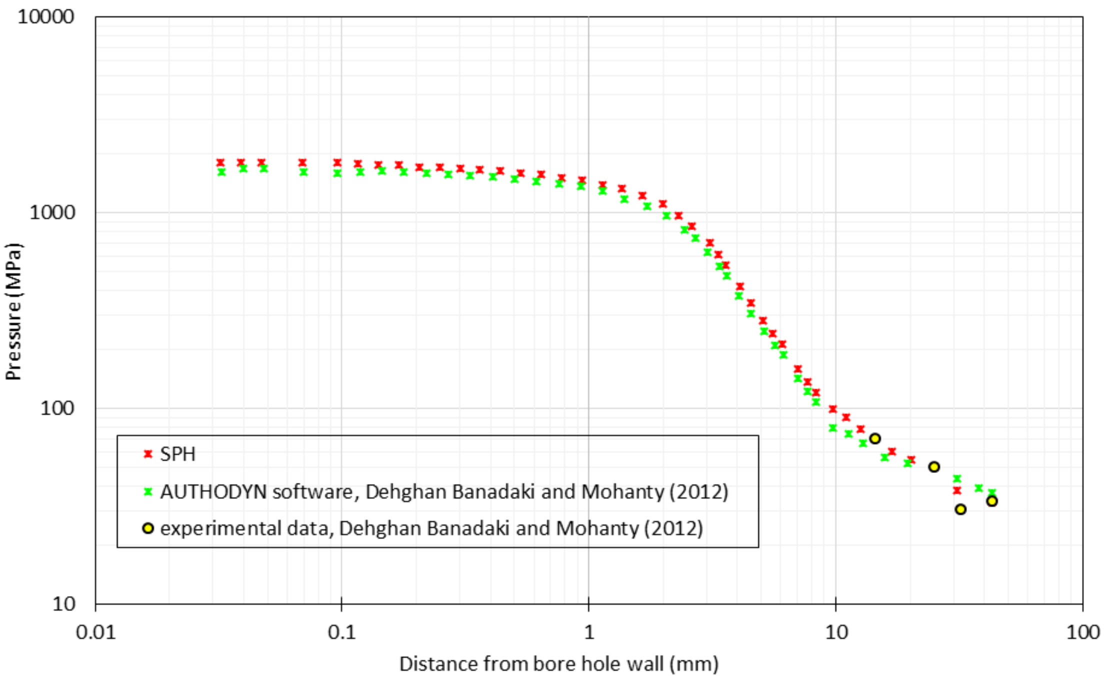

Figure 4. Comparison of pressures at different distances from the borehole walls obtained from experimental and numerical works.

In order to further validate our simulations with experimental data, damage distribution around the borehole was examined qualitatively. Exploded rock was cut at 25, 75 and 125 mm from the bottom surface of the rock specimen in experimental test. Figure 5 compares fracture patterns for the air-coupled with copper simulation. As seen, after explosion the resulted intense stress wave travels into the rock specimen and causes different types of failures. To investigate the formation mechanism of the different types of failures, the relationship among pressure, stresses and strength for the failed particles are presented. In the three failed particles as shown in Figure 5, the histories of stresses are recorded in order to analyse rock fracture mechanism. Throughout this work, tensile stress is positive and compressive stress is negative.

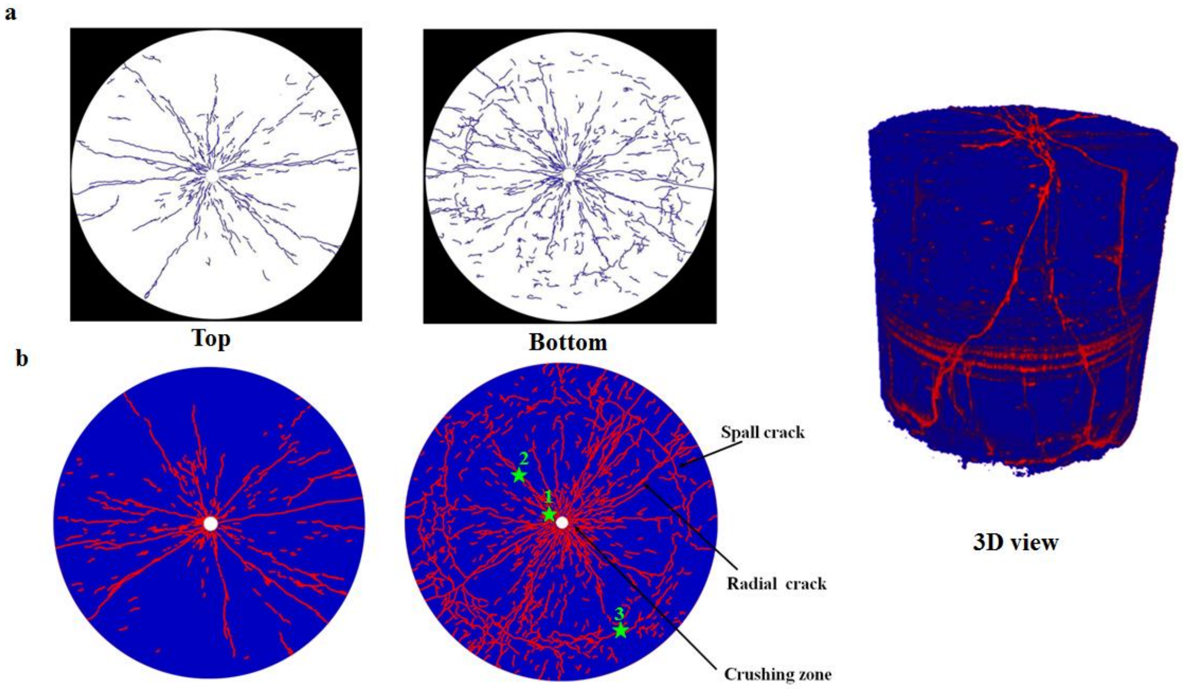

Figure 5. Comparison of damage created around the borehole for top and bottom sections, a) experimental [22], b) numerical simulation.

For the failed particle close to the borehole wall ($x = 8.54$ mm, $y = 4.43$mm, $z = 100$ mm) at times smaller than 72.5 μs, before the shock wave touches this particle, the particle pressure is equal to zero and yield stress is equal to 286 MPa (see Figure 6). Details of obtaining the yield stress can be found in [17, 18]. Then yield stress gradually increases with pressure and reaches its maximum value of 2499 MPa at 72.754 μs. As expected for the JH2 model, this clearly shows the pressure dependency of the strength. Rock behaves elastically from when it experiences the shock wave until the Mises stress contacts the yield surface. After the peak pressure has passed the particle, Mises stress contacts the yield surface at time 72.83 μs and the particle starts to deform plastically. During plastic deformation damage accumulates in the particle. Maximum and minimum principal stresses increase with time at the compressive status. At 72.8 μs, the maximum shear stress reaches up to 853.17 MPa, which is much larger than the rock dynamic shear strength (265 MPa). Then the particle fails in shear, and the all principal stresses, pressure, Mises stress and yield stress fall to zero.

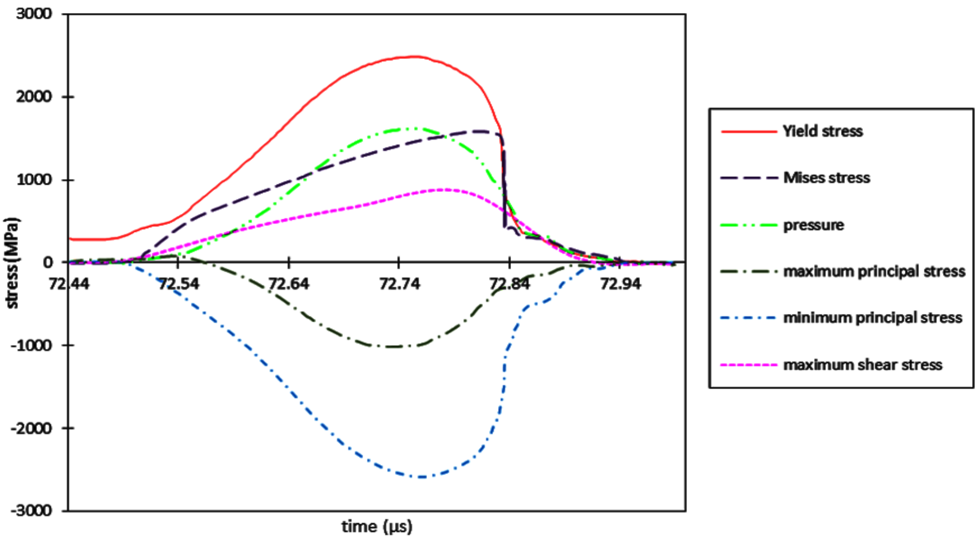

Figure 6. Relationship between pressure, stresses and strength versus time for failed point 1 close to the borehole (shown with a green star in Figure 5).

The failed particle in coordinate of ($x = 31.75$ mm, $y = 28.62$ mm, $z = 100$ mm) is selected to investigate the radial crack formation. The pressure, stresses and strength as a function of time are shown in Figure 7. Like previous case, Mises stress contact the yield surface after the passage of the compressive stress wave at time 73.61 μs. The tension tail of the compressive stress wave results in negative pressure in the particle followed by positive pressure. The minimum principal stress is always compressive stress. The maximum principal stress alternates between compression and tension status due to the coupling effect between the stresses and particle strain energy release; then it reaches 115 MPa at 73.43 μs, which is larger than the rock dynamic tensile strength (100 MPa) cause the tensile failure at this particle. The maximum shear stress doesn't exceed the dynamic shear strength of rock so the mechanism of failure cannot be in shear. Then when particle completely damaged all the stresses become zero.

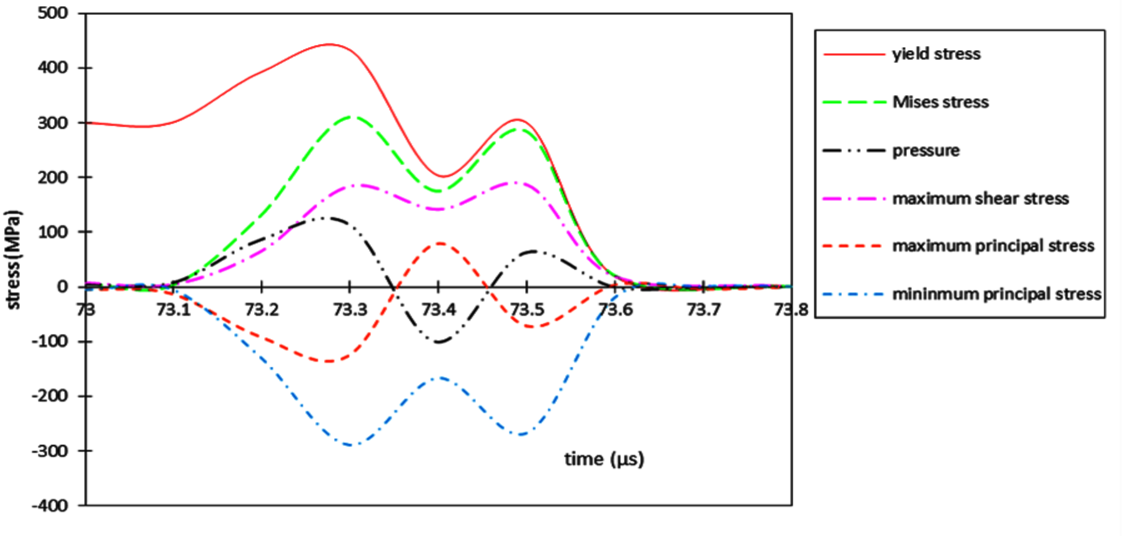

Figure 7. Relationship between pressure, stresses and strength versus time for failed point 2 (shown with a green star in Figure 5).

The relationships between pressure, stresses and strength for particle on the spall crack at position of ($x = 68.23$ mm, $y = -57.98$ mm, $z = 100$ mm) are shown in Figure 8. Unlike the previous cases, Mises stress does not contact the yield surface after the passage of the compressive stress wave. The stress wave propagates to the particle at 76.87 μs; then, the principal stresses increase with time at the compressive status. The maximum principal stress reaches 107 MPa at 87.65 μs, and the particle fails in tension. After a while, the reflected wave comes back from the free surface resulted in higher negative pressures in the selected particle. Although the particle fails because the maximum principal stress exceeds the rock dynamic tensile strength, its maximum shear principal stress is not close to the rock dynamic shear strength at this time. Thus the failure is not in shear. These results are in good agreement with work [22]. Experiments on rock also show similar signs of damage (Figure 5).

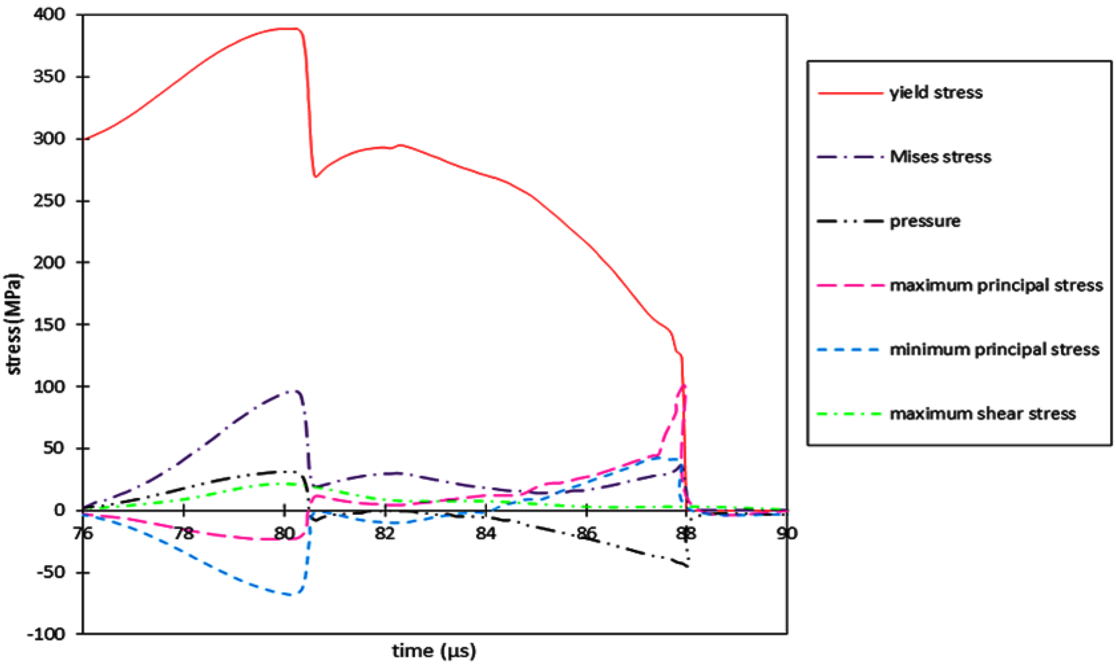

Figure 8. Relationship between pressure, stresses and strength versus time for failed point 3 (shown with a green star in Figure 5).

In Figures 6, 7 and 8, when the Mises stress becomes larger than the intact strength, it returns back to the yield surface and rock undergoes plastic deformation. With increasing permanent deformation, damage in the material accumulates and its strength gradually decreases from the intact strength to a lower strength [19].

In order to quantify the variations of crack patterns in their experimental tests, crack densities, defined as length of cracks per unit area, were calculated at different depths and radial distances from the specimen borehole [22]. Each image was then calibrated spatially and divided into three equal width zones from the centre to the edge with zone 1 being in the centre and zone 3 the most outside. Crack densities were then calculated by dividing the total length of all the cracks in each category by the zone area.

In calculating the crack density, each SPH particle is considered occupy space of a cube with size of 0.15 mm. The following equation was used to calculate the crack density

$$\Gamma = \frac{\sum_{i}^{n} D_i \times A_i^{1/2}}{A_{zone_j}} = \frac{L_i \times \sum_{i}^{n} D_i}{A_{zone_j}} \tag{12}$$

where Γ, D_i, L_i, A_i and $A_{(Zone\ j)}$ are crack density, the damage of particle *i*, length of particle *i*, area of particle *i*, area of zone *j*. In this work, any particle with D>0.8 is considered crack.

Figure 9 shows the crack density in Barre granite for water-coupled and air-coupled with and without copper as well as the variation of measured crack densities for top, middle and bottom surfaces of rock, respectively. Crack density was measured in terms of mm/mm^2. Investigation of the crack patterns on cross sections of rock (Figure 5) reveals that by moving from top to the bottom of the specimen, the number of smaller cracks and the number of longer cracks are increased. This is related to the stronger stress field, due to confinement at greater depths, at distances away from the top surface of the specimen.

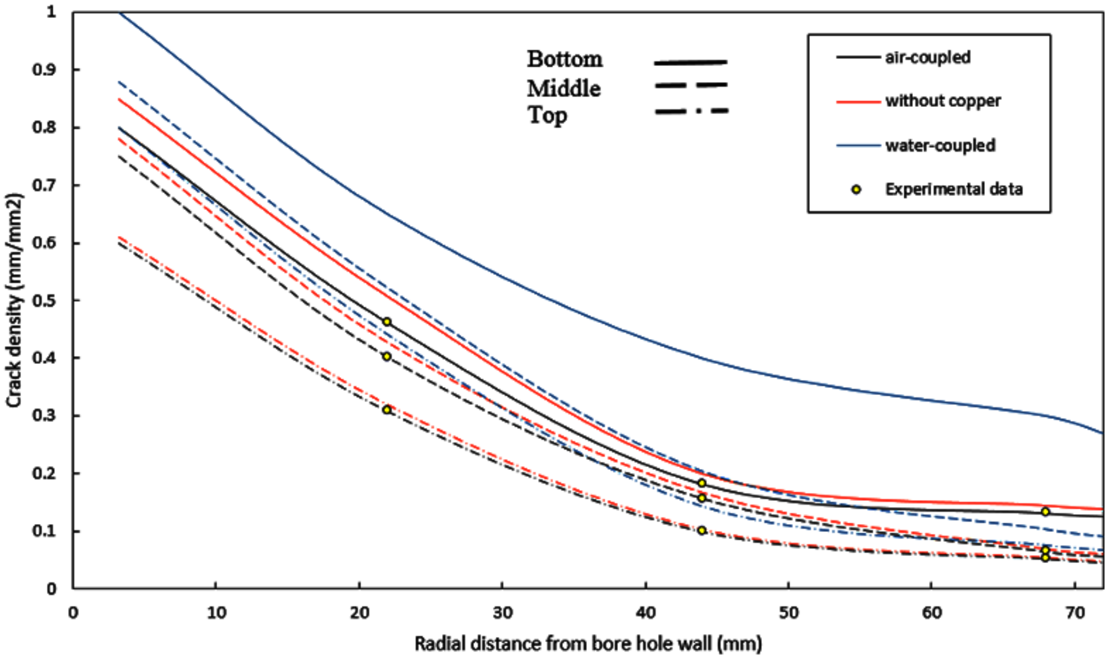

Figure 9. Variation of crack density in radial and axial directions of rock for experimental [22] and three simulations.

It is seen that for the three cross sections of rock, crack densities around the borehole are much higher than far distances from the borehole. This is not surprising since the rock adjacent to the borehole experiences higher stress intensities. On the other hand, maximum crack density is observed at the bottom region of rock. Close to the borehole, the difference between crack densities is minimum. In fact, near the borehole crack densities at top, middle and bottom regions are very similar. As shown in Figure 9, our simulations match well with the experimental results.

The difference in crack density from simulations with and without copper was observed to be marginal, especially at the top and mid-sections of the specimen, while a noticeable difference was noted at bottom section closer to the borehole. The number of damaged particles in bottom section for two simulations of air-coupled with and without copper are shown in Figure 10. The induced damage rate for simulation without copper is much higher than that with copper. The rate of damaged particle generation is reduced as the redial cracks gradually lose their initial momentum to extend. This is suggested by the drastic difference in the slopes of the Figure 10. The difference between the number of damaged particles for simulations with and without copper is the kinetic and elastic strain energies that are absorbed by the copper as a liner.

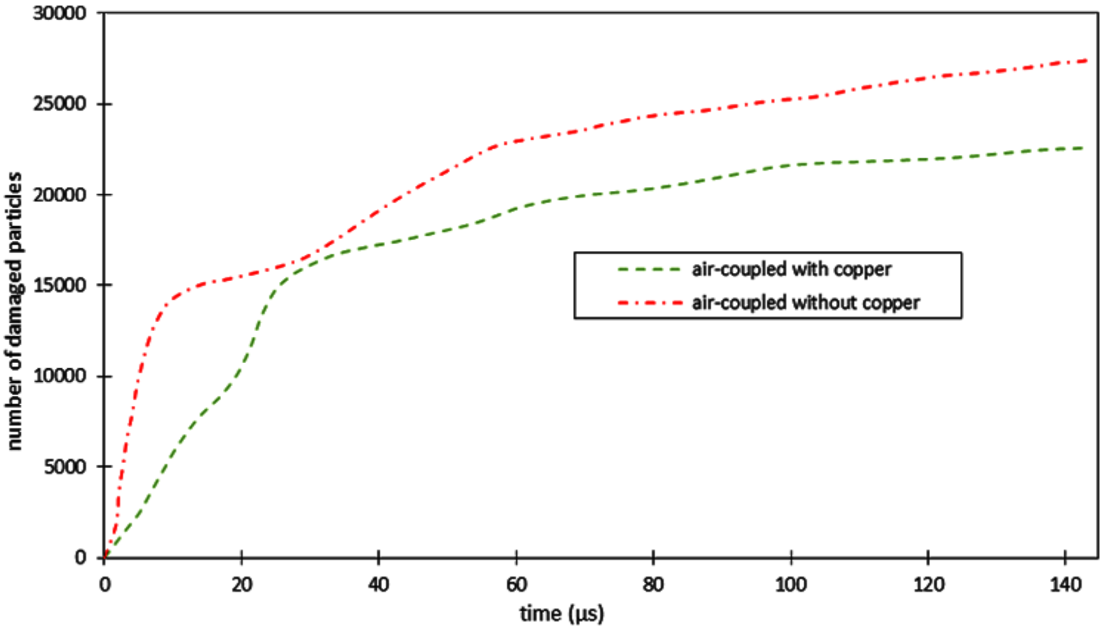

Figure 10. Number of damaged particles in bottom section for air-coupled simulation with and without copper.

Crack density is much higher for the water-coupled case in comparison with air-coupled case with and without copper. This is to be expected, as water is known to serve as an excellent medium for transmission of shock and stress wave, compared to air.

Crack distribution probability

Crack distribution probability is approximated by a function defined on damage level and number of damaged particles for comparison in radial direction. In this method, each cross section with normal direction along the Z axis, is divided into 72 segments with the bin size of 5 degree. Then the number of particles with damage level equal to or above 0.8 is counted and divided by the total number of damaged particles in that cross section.

$$PDF = \frac{\sum_i^n D_i}{\sum_i^{72}\sum_i^n D_i}\frac{1}{bin/360} \tag{13}$$

where *PDF* is probability distribution function and *n* is the number of damaged particles. For comparison of different simulations, PDF function is normalized.
Figure 11 shows the polar graphs which compare the normalized crack distribution probability for three simulations air-coupled, without copper and water-coupled from time 23 μs to 144.88 μs. It can be clearly seen that the normalized probability at time 23 μs in all direction (0^o-360^o) around the borehole is the same for these three simulations. The normalized probability for air-coupled, without copper and water-coupled are 0.000942,

0.001682 and 0.003558, respectively. At time 69 μs, the normalized probability is different from 0° to 360° direction around the borehole for three simulations, however, this distribution shows a symmetrical pattern around the borehole. The same results at time 69 μs are obtained for without copper and water-coupled simulations.

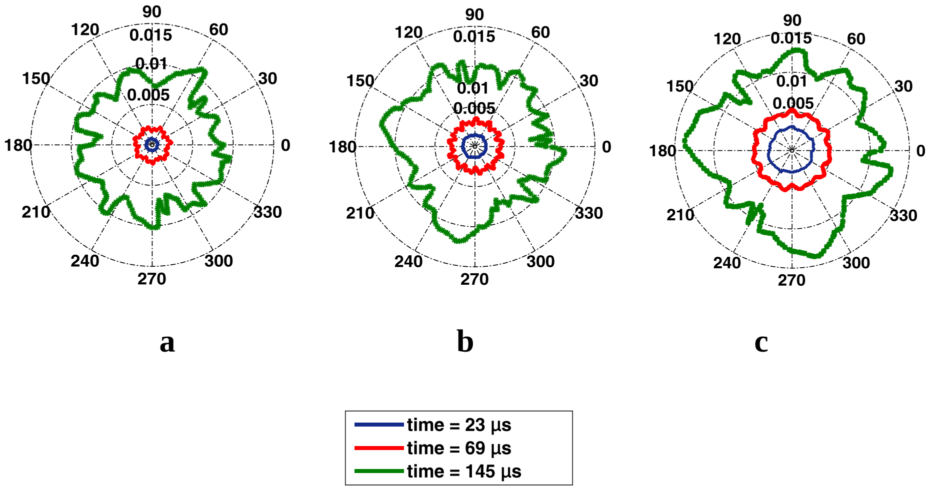

a **b** **c**

Figure 11. Normalized crack distribution probability in bottom section a) air-coupled b) without copper c) water-coupled.

At time between 69 μs and 144.88 μs, the normalized probability distribution shows an asymmetrical patterns around the borehole for three simulations. This is mainly due to the specific failure criterion applied. In the simulation, if a particle is failed, it will not be able to sustain any tensile and shear loadings, i.e., its tensile and shear stresses will release, which will significantly affect the stress field around this failed particle, therefore, the particle stresses could be different. Therefore, stress interaction between a fracture and a field of cracks in the three dimensional space generate irregular fracture pattern. It can be seen that the resulting probability distributions are quite different each other. Water-coupling produces the most extended crack zones probability, and air-coupling the least.

Conclusions

This study presented an approach that allows the prediction of 3D fracture structure under different blast loading by SPH method. The validity and predictability of models obtained by comparing fracture patterns to experimental works. The main conclusions are:

(1) It is found that the SPH simulations with the JH2 model are very promising in effectively elucidating the complicated and fundamental failure mechanisms of rocks. The more accurate type of simulation has been made possible by the development of the SPH method.

(2) Adopted SPH method permits the 3D quantification of the fracture patterns. The quantification results are in satisfying agreement with experimental measurements.

(3) The study showed that radial cracks propagate along different directions with different distributions and the propagation direction. The crack distribution probability was found to be asymmetrical around blast hole. Numerical results show that densely cracked region around the borehole, radial and spall cracks match well with experimental results. The agreement is both qualitative and quantitative.

Acknowledgments

The work was supported in part by the Australian Research Council through Discovery Projects (DP140100945 and DP170102886) and by the National Natural Science Foundation of China (Grant No. 11232003). This research was undertaken with the assistance of resources and services from the National Computational Infrastructure (NCI), which is supported by the Australian Government.

References

[1] Sarbhukan, M. M. (1990) Application of Bore - Blast technique for rock fracturing for drinking water: A case study of Ghotkarwadi, Taluka Akole District Ahmednagar. Proceedings of national seminar on Modern techniques of rain water harvesting, water conservation and artificial recharge for drinking water, afforestation, horticulture and agriculture, Government of Maharashtra (India), pp. 827-838.

[2] Stephens, D. R. (1974) Revised cost estimate for the LLL in-situ coal gasification concept. Lawrence Livermore Laboratory, Livermore, Calif., Rept. UCRL-51578.

[3] Austin, C. F. and Leonard, G. W. (1973) Chemical explosive stimulation of geothermal wells. Geothermal Energy Resources, Production and Stimulation, Stanford U. Press, Stanford, Calif. 269-292.

[4] Miller, J. S., Walker, C. J., and Eakin, J. L., (1974) Fracturing oil shale with explosives for in-situ oil recovery. USBM, Bartlesville, Okla., Rept. RI 7874.

[5] Zhu, Z., Xie, H., Mohanty, B. (2008) Numerical investigation of blasting-induced damage in cylindrical rocks. International Journal of Rock Mechanics and Mining Sciences **45**, 111-121.

[6] Shin, YS., Chisum, JE. (1997) Modelling and simulation of underwater shock problems using a coupled Lagrangian-Eulerian analysis approach. *Shock and Vibration* **4**, 1–10.

[7] Potyondy, D., Cundall, P., Sarracino, R. (1996) *Modelling of shock- and gas-driven fractures induced by a blast using bonded assemblies of spherical particles.* Rock fragmentation by blasting. Rotterdam, Netherlands: A.A. Balkema. p. 55–62.

[8] Trivino, L.F.n., Mohanty, B. (2015) Assessment of crack initiation and propagation in rock from explosion-induced stress waves and gas expansion by cross-hole seismometry and FEM–DEM method. *International Journal of Rock Mechanics & Mining Sciences* **77**, 287–299.

[9] Libersky, L.D., Randles, P.W., Carney, T.C., et al. (1997) Recent improvements in SPH modelling of hypervelocity impact. *International Journal of Impact Engineering* **20**, 525–532.

[10] Chen, Z., Hu, W., Shen, L., Xin, X., and Brannon, R. (2002) An Evaluation of the MPM for Simulating Dynamic Failure with Damage Diffusion, *Engineering Fracture Mechanics* **69**, 1873-1890.

[11] Flores-Johnson, E.A., Wang, S., Maggi, F., El-Zein, A., Gan, Y., Nguyen, G.D., and Shen, L. (2016) Coupled discrete element – finite element method for modelling dynamic impact of unsaturated sand. *International Journal of Mechanics and Materials in Design,* **12**(4), 495-507.

[12] Pramanik, R. Deb, D. (2014) Implementation of Smoothed Particle Hydrodynamics for Detonation of Explosive with Application to Rock Fragmentation. *Rock Mechanics Rock Engineering* **16**, 92–99.

[13] Gharehdash, S., Shen, L., Gan, Y., Flores-Johnson, E. A. (2016) Numerical Investigation on Fracturing of Rock under Blast Using Coupled Finite Element Method and Smoothed Particle Hydrodynamics. *Applied Mechanics and Materials* **846**, 102-107.

[14] Fakhimi, A., Lanari, M. (2014) DEM–SPH simulation of rock blasting. *Computers and Geotechnics* **55**, 158–164.

[15] Gingold, R., Monaghan, J. (1977) Smoothed particle hydrodynamics theory and application to non spherical stars. *Monthly Notices of the Royal Astronomical Society* **181**, 375–389.

[16] LS-DYNA LSTC. (2010) *keyword user's manual*, Version 970, Livermore Software Technology Corporation, Livermore, CA.

[17] Monaghan, J. (2000). SPH without a Tensile Instability, *Journal of Computational Physics* **159**, 290 311.

[18] Rabczuk, T., Belytschko, T., Xiao, SP. (2004) Stable particle methods based on Lagrangian kernels. *Computer Methods in Applied Mechanics and Engineering* **193**, 1035–63.

[19] Johnson, GR., Holmquist, TJ. (1999) Response of boron carbide subjected to large strains, high strain rates, and high pressures. *Journal of Applied Physics* **85**, 8060–73.

[20] Dehghan Banadaki, M.M., Mohanty, B. (2012) Numerical simulation of stress wave induced fractures in rock. *International Journal of Impact Engineering* **41**, 16-25.

[21] Johnson, G.R., Cook. W.H. (1983) *A constitutive model and data for metal subjected to large strains, high strain rates and high temperature.* In Proceedings of the 7th International Symposium on Ballistics. The Hague, Netherlands.

[22] Dehghan Banadaki, MM. (2010) *Stress-wave induced fracture in rock due to explosive action*. PhD thesis. Canada: University of Toronto.